International Journal of Innovative Research and Scientific Studies, 8(2) 2025, pages: 2820-2833

IJIRSS
International Journal of Innovative Research & Scientific Studies

ISSN: 2617-6548

URL: www.ijirss.com

Conical waveguide design for propagating light to a single fiber and its indoor characterization methodology

Ricardo Chapa-Garcia[1], Daniel Toral-Acosta[2], Romeo Selvas-Aguilar[1*], Juan Luis López-Diaz[3], Luis Fernando Enriquez-Gomez[4]

[1]*School of Mathematical and Physical Science, Autonomous University of Nuevo Leon, San Nicolas de los Garza, Nuevo Leon, Mexico.*
[2]*SECIHTI-FCFM, Autonomous University of Nuevo Leon, San Nicolas de los Garza, Nuevo Leon, Mexico.*
[3]*Center for Innovation in Applied Engineering, Catholic University of Maule, Talca, Chile.*
[4]*Faculty of Mechanical and Electrical Engineering, Autonomous University of Coahuila, Ejido El Aguila, Torreon, Coahuila, Mexico.*

Corresponding author: Romeo Selvas-Aguilar (*Email: romeo.selvasag@uanl.edu.mx*)

Abstract

This study introduces a novel optical setup and methodology to increase the effective area of a multimode optical fiber (MMF) using a low-cost, 3D-printed conical waveguide (CW). Designed to simplify solar collection systems with Fresnel lenses (FL) and optical fibers, the setup efficiently couples light into a single silica MMF. For this, an indoor characterization method assesses transmission efficiency, verifying in advance its suitability for outdoor use while minimizing sun exposure risks for the people conducting the experiments. A laser flashlight provides a collimated light source with approximately 2° divergence for experiments. Geometric analysis and ray-tracing simulations validate the CW design, highlighting the importance of a low FL numerical aperture (NA). By reducing the FL's NA to 0.11 using masks, a maximum CW's transmittance of 34.7% and a net system efficiency of 17% are achieved. Key advantages include simplified assembly, avoiding the complexities of fiber bundle manufacturing, low optical attenuation over tens of meters, and safe indoor characterization. This approach presents a solution for compact photonic energy transport systems and provides a reference framework for identifying improvements to the collection system. The findings of this study are intended for use in a sunlight collector device for indoor lighting.

Keywords: Conical waveguide, Fresnel lens, Indoor optical setup, Laser flashlight, Light collection-transmission, Multimode fiber, Ray-tracing simulations.

DOI: 10.53894/ijirss.v8i2.5820
Funding: This study received no specific financial support.
History: Received: 19 February 2025 / **Revised:** 19 March 2025 / **Accepted:** 22 March 2025 / **Published:** 1 April 2025

Competing Interests: The authors declare that they have no competing interests.
Authors' Contributions: All authors contributed equally to the conception and design of the study. All authors have read and agreed to the published version of the manuscript.
Transparency: The authors confirm that the manuscript is an honest, accurate, and transparent account of the study; that no vital features of the study have been omitted; and that any discrepancies from the study as planned have been explained. This study followed all ethical practices during writing.
Acknowledgments: The authors thank CONAHCYT-SECIHTI for the scholarships given.
Publisher: Innovative Research Publishing

1. Introduction

Nowadays, renewable energy must be widely adopted to reduce the global impact of pollution caused by fossil fuel consumption [1, 2]. Approximately 30 percent of global energy consumption takes place in buildings, primarily for heating, cooling, cooking, and lighting [3]. Artificial lighting alone accounts for about 13 to 20 percent of global electricity consumption, and lighting-related greenhouse gas emissions represent approximately 5 to 7 percent, primarily due to fossil fuel consumption and flaring in recent years. Consequently, countries recognize the need to invest in renewable energy and promote innovative solutions and developments aimed at harnessing solar energy [4-11].

Efficient indoor lighting is a critical aspect of building design, significantly affecting both energy consumption and occupant well-being [12, 13]. Integrating natural daylight into buildings can enhance productivity and create a pleasant working environment. However, the variability of natural light presents challenges in maintaining consistent indoor lighting levels. To address these challenges, recent research has focused on developing advanced daylighting systems that combine natural and artificial light sources[11, 14-19].

Numerous theoretical studies, simulations, and experimental tests have been conducted to examine the phenomena involved in light transmission [20]. These studies employ various setups, arrangements, or configurations, primarily utilizing optical elements such as Fresnel lenses, optical fibers, and waveguides. Below, we present some research related to this field:

The study "The Limits to Incoherent Optical Power Launching into Light Guides" compiles and analyzes theoretical limits and potential practical techniques for optimizing light launch from incoherent sources into large-diameter light guides [21].

Another study by Viera-González, et al. [22] presents a radiant flux analysis of an imaging-based system, using geometrical optics and simulations in the software Zemax OpticStudio.

In Arnaoutakis, et al. [23] the results of ray-tracing simulations for a novel two-stage solar concentrator coupled with an optical fiber are compared to experimental measurements. The study optimizes coupling efficiency by analyzing the focal ratio and acceptance angle of the primary and secondary concentrators, respectively. The research in Vu, et al. [24] presents a new design for a large-scale spectral splitting concentrator photovoltaic system based on dual flat waveguides. The sunlight concentrator consists of a Fresnel lens array paired with dual waveguides, and the system model was developed using LightTools software.

To perform the theoretical analysis, simulations, and experiments in the previous works, the light rays emitted by the sun or artificial light sources that simulate the light rays were considered. In this research, a novel optical setup and methodology for increasing the effective area of a multimode optical fiber (MMF) were developed by designing and implementing a genuine conical waveguide (CW) with a low-cost manufacturing process. This approach enables a configuration in which light collected by a Fresnel lens (FL) can be coupled into a single MMF spliced to the output of the CW.

The CW acts as a secondary optical element (SOE), receiving a focused beam from the FL. The focused beam spot size (BSS) fits within the base area of the CW cone. The transmitted light exits from the CW's output (top area), which has a smaller cross-sectional area that matches the core size of the receiving 1 mm silica MMF. Furthermore, it offers low optical losses over distances of several tens of meters.

Additionally, this setup allows an indoor characterization to determine the collector's light transmission efficiency and assess in advance whether it would be viable for outdoor use. It also helps avoid prolonged sun exposure to people involved in experiments of this type. These experiments can typically take from 1 to 6 hours per day due to setup, initiation, monitoring, measurement, and data capture, which can lead to heatstroke, skin diseases, or other health issues [25-30]. Therefore, an exhaustive investigation had to be conducted on reasonably collimated artificial light sources that resemble sunlight rays. Initially, light emitter diode (LED) sources and lens arrays were used to collimate the light [31, 32].

However, the resulting beam divergence was large and significantly exceeded the surface of the FL collector, and the focused beam spot wasn't small enough for the purposes of this research. Therefore, a laser emitter phosphor (LEP) technology source was chosen, which provided a light beam with better collimation and matched the beam size required to cover the FL surface [33-38]. Its low ~2° divergence, was crucial for its use as a light source in this research. Using this source, several FLs were tested, producing a focused BSS ranging from 3 to 6.5 mm in diameter.

Using the previously described setup, a geometric analysis was conducted, initially based on the concept of étendue, which provided reference points for selecting the characteristics of the fiber lens (FL), specifically its numerical aperture (NA) and focused beam size (BSS), that best fit the NA and core size of the chosen multimode fiber (MMF). Following this, the dimensions of the coupling waveguide (CW) were proposed, and the analysis involved calculating the number of reflections each ray could experience before it no longer met the Total Internal Reflection (TIR) condition within the CW. Additionally, a ray-tracing simulation of the CW was then conducted to verify the transmission efficiency.

The luminous flux measurements showed that the highest efficiency at the CW output was approximately 34.7%, while at the MMF output it was around 17%. The results were consistent with the behavior predicted by the simulations and the geometric analysis.

2. Materials and Methods

The diagram in Figure 1 (a) illustrates the arrangement of the components, where the CW functions as a SOE in a light collection system based on a FL and an MMF. In collection systems like this, fibers typically have a high numerical aperture and large diameters to provide a cross-sectional area sufficient to capture light focused by a relatively large-diameter lens. In our case, the chosen MMF is a 1-mm-diameter silica optical fiber with core and cladding diameters of 1000 μm and 1080 μm, respectively (Thorlabs model FP1000URT). This MMF is a step-index type with a 0.5 NA and core/cladding refractive indices of 1.4584 and 1.3651 at 589 nm, respectively. This MMF was selected after evaluating cost against core size, as it offered a reasonably low cost per meter.

The FL was selected based on having a relatively low NA, and a focused BSS < 5 mm, since larger spot sizes would complicate the coupling of light first into the CW and subsequently into the MMF. After preliminary tests with various lenses was determined that a FL from Edmund Optics (refractive index = 1.49) with the following specifications was suitable: effective size of 21.59 cm x 26.67 cm, focal length = 45.72 cm, NA = 0.229, and a transmission efficiency of 85%. Based on these criteria, the CW diameters were set to 5 mm at the base and 1 mm at the tip, leaving only the cone height to be determined to complete the geometric design.

For ease of fabrication and cost-effectiveness, epoxy resin with a refractive index of ~1.49 was selected as the material for the CW. The proposed setup directs a focused beam (BSS < 5mm) from the FL into the CW via TIR, exiting through the cone tip. The CW and MMF core diameters match for easy splicing using UV-curing adhesive. A ray-tracing optic model suffices to analyze the system under typical conditions (V-number > 5000 at 589nm).

2.1. Geometric Analysis

As illustrated in Figure 1 (b), two marginal rays enter into the CW; they represent the envelope of the focused beam coming from the lens. If these rays have an angular aperture that meets the critical angle requirement within the CW, they can propagate as TIR rays toward the tip of the cone. Upon entry, the inclined sidewalls of the CW cause the reflected rays to become progressively more oblique.

For the rays exiting through the tip of the CW to be successfully coupled into the receiving MMF, they must fall within the acceptance cone of the fiber. As shown in Figure 1 (b), this acceptance cone has an apex angle, denoted by θ_{fiber}= 60°, which corresponds to the 0.5NA of the fiber. Any angular aperture larger than this value will result in rays that cannot be coupled into the MMF. To maximize the system's efficiency, it is essential to operate under conditions that approach an overfilled launch into the fiber.

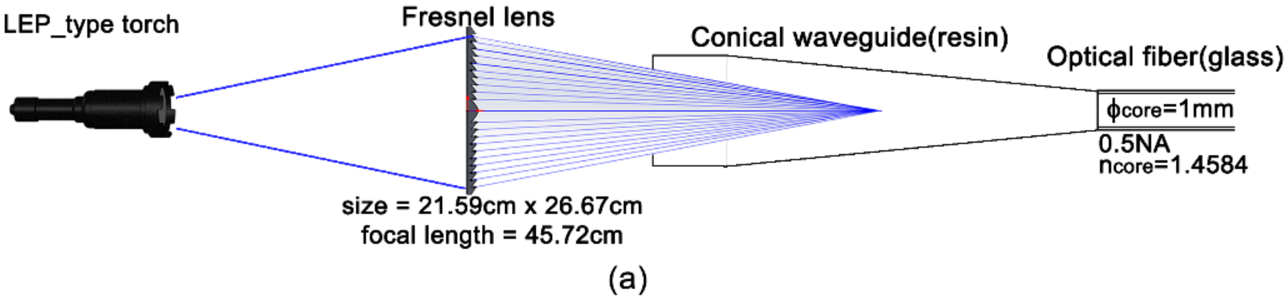

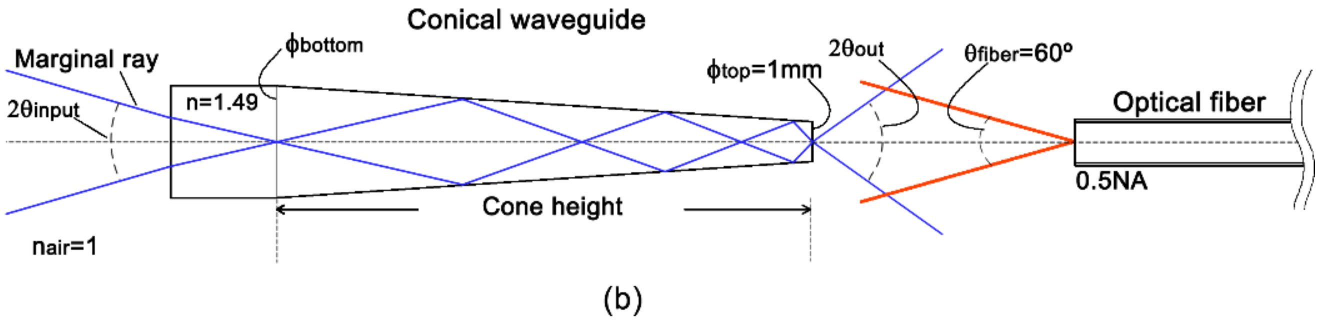

Figure 1.
(a) Experimental setup of the proposed light collection system; (b) Increase in the input/output angular aperture illustrated by two marginal rays propagating within the CW.

The light losses expected in this collector system, are directly related to the concept of etendue, which can only be conserved or increased. According to the general definition of etendue Brooker [39] we can establish the following conservation equation for etendue, which applies to the geometric conditions of a system aligned along the optical axis:

$$A_1 NA_1^2 = A_2 NA_2^2 , \tag{1}$$

where A_1 is the area of the focused BSS at CW base, and A_2 correspond to the CW tip area, while NA_1, NA_2 can be defined as follows: i) NA_1= $n_{\text{air}}\sin\theta_{\text{input}}$ and is equivalent to the FL´s NA. ii) NA_2= $n_{\text{air}}\sin\theta_{\text{out}}$ which corresponds to the light cone exiting the CW through its tip. In our case, Equation (1) allows us to explore combinations of areas and angular apertures for the rays entering and exiting the CW, which could potentially achieve ideal efficiency, meaning that optical power is preserved.

In the following example, we will use the areas A_1 and A_2, as well as NA_1 in Equation (1), to determine the value of NA_2 that would conserve etendue.

These areas correspond to the focused BSS and the diameter of the CW's tip. We will assume a BSS of approximately 4 mm diameter, as we want it to be smaller than the diameter of the cone's base. For NA_1, we will initially use the original 0.23NA of the FL. With these three known values, we can estimate NA_2=0.92.

This value significantly exceeds the 0.5NA of the MMF, meaning the CW's output cone is larger than the MMF acceptance cone. To reduce losses, lower NA_1 values can be introduced by using masks on the original FL to create a smaller aperture, then, by maintaining the same focal length, this methodology enables the reduction of NA_1, as the diameter decreases due to the masks. In particular we use three different masks with aperture diameters of 10 cm (0.11NA), 15 cm (0.162NA), and 20 cm (0.213NA), respectively.

Table 2 summarizes the NA_2 values that result from using different NA_1 values while keeping the input and output diameters constant. Notably, the table entry with NA_2=0.436 indicates that all light exiting the CW remains within the acceptance cone of the receiving MMF (NA_2<0.5).
However, we can experimentally explore the areas and numerical apertures according to the values in Table 1, and with the initial constraints given by the focused BSS and CW tip diameters, a cone height can be defined so that the CW's output NA reasonably match with the MMF's NA for a better light coupling. Any observed losses in the measurements will simply represent deviations from the ideal conditions indicated by Equation (1).

Table 2.
Comparison of input and output diameters and apertures of the CW with constant etendue.

$\phi 1$	$\phi 2$	NA_1	NA_2
4mm	1mm	0.23	0.92
4mm	1mm	0.213	0.852
4mm	1mm	0.162	0.648
4mm	1mm	0.109	0.436

Figure 2 is a 2D representation of the CW, showing two marginal incident rays on the base of the CW. These rays represent the envelope of the beam focused by the FL. Although five reflections are depicted, this is for illustrative purposes only, as the aim of this representation is to determine the conditions that the marginal rays must meet to propagate by TIR all the way to the tip.

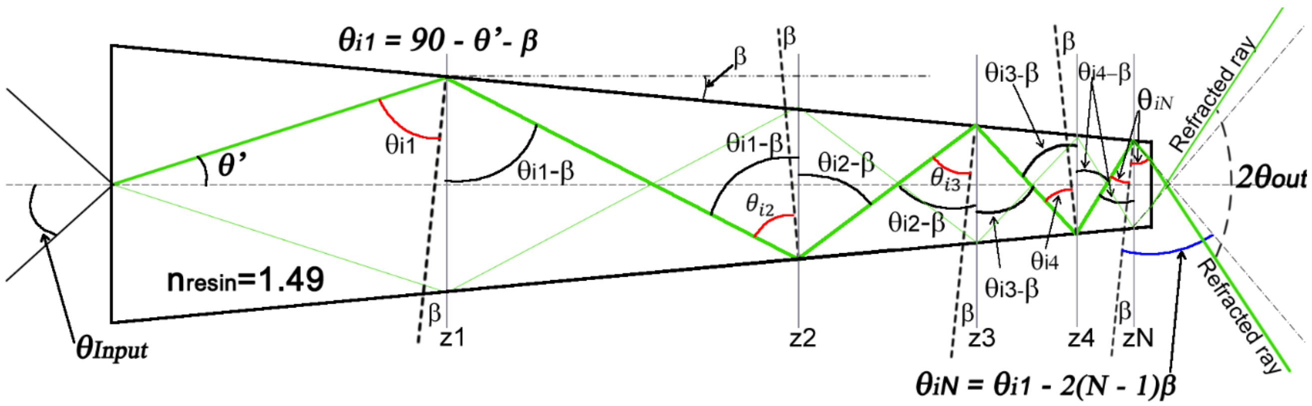

Figure 2.
2D sketch of a pair of marginal rays propagating via TIR along the CW.

The pair of marginal rays entering the CW undergo successive TIRs, with each reflection resulting in a gradual reduction of their angle with respect to the normal (θ_{i1}, θ_{i2}, θ_{i3}, etcetera). After N reflections, the angle will have decreased to a value given by:

$$\theta_{iN} = \theta_{i1} - 2(N-1)\beta, \qquad (2)$$

where β is the slope angle of the cone's sidewall. This trend means that, eventually, some rays initially guided within the CW will no longer satisfy the CW´s critical angle condition. From Figure 2, It may be observed that Equation (2) was applied with the N-reflected ray at the end of the CW, therefore N=5. Nevertheless, in order to calculate the reflection angle at different positions within the CW, one can enter a different value for N. It is worth noting that the critical angle value is independent of β and can be determined using Snell's law as $n_{resin}\sin\theta_{CW\_crit}=n_{air}\sin 90°$, giving θ_{CW_crit}= 42.14° in which n_{air}=1 and n_{resin}=1.49 respectively.

On the other hand, all rays that exit through the tip of the cone will be confined within a cone of light with an angular aperture $2\theta_{out}$. The corresponding MMF's acceptance cone is (see Figure 1 (b)) θ_{fiber}= 60°. From the previous discussion on etendue (see Table 2), it is very likely that under typical operating conditions $2\theta_{out}$>θ_{fiber}. As a result, only those rays that do not exceed this angle will be coupled into the fiber, once the corresponding splice is made.

While this MMF is not shown in Figure 2,, we know that the previous mentioned angular condition is sufficient to ensure bound rays into the MMF. This essentially means that once a ray enters the MMF and reflects for the first time within the fiber wall, it will continue to be guided as long as its angle relative to the normal (at the core-cladding interface) is greater than or equal to θ_c^{MM} which is the MMF´s critical angle. Additionally, it should be noted that θ_{iN} depends on θ_{input} and FL´s NA. This aperture will be adjusted by applying the masks mentioned earlier to vary NA_1 according to the cases in Table 2.

Based on the preceding geometric analysis, we can propose as a starting point, a 50 mm cone height, from which we can determine a slope angle of β=2.29° and θ_{iN}. These values are useful to estimate the number of reflections that a marginal ray (with θ_{input}) can undergo before experiencing attenuation due to Fresnel reflection at the cone's sidewall. Although this height is not optimal, it is long enough to produce a small β angle while still being short enough to avoid excessive number of reflections before reaching the cone's tip. Selecting an intermediate value of NA_1=0.162 from Table 2, we can calculate θ_{iN}.

This exercise aims to answer two questions to understand the CW performance. First, how many reflections a marginal ray will experience before it starts to attenuate due to Fresnel reflection at the sidewall ($\theta_{iN} \leq \theta_{\mathrm{CW\_crit}}$). Second, how many reflections a marginal ray can undergo within the CW before its angle θ_{iN} reaches MMF´s critical angle θ_c^{MM}= 69.9° (obtained from fiber specs).

With reference to Figure 2 and knowing that NA_1= $n_{air}\sin\theta_{input}$, we apply Snell's law to determine $\theta' = 6.24°$ and consenquently $\theta_{i1} = 81.47°$, then using Equation (2) we can estimate that a marginal ray (for 0.16NA) could maintain up to 9 TIRs (N=9) before it begin to attenuate due to Fresnel reflection loss. Therefore, for the tenth reflection θ_{i10} =40.25° < $\theta_{\mathrm{CW\_crit}}$=42.14° which is lower than the critical angle, preventing further propagation via TIR.

This calculation determines the number of TIR´s based solely on the angle β and is shown for comparative purposes. It is not relevant whether the distance z (z_1, z_2, etcetera) traveled exceeds the cone length in this assumption; what matters is determining the CW escape threshold given the FL´s NA.

Similarly, we can calculate how many TIR´s a marginal ray can undergo before its angle θ_{iN} approaches the value θ_c^{MM}= 69.9°. Assuming N=5, then θ_{i5}= 63.15°. This means that for a marginal ray with the same input angle θ_{i1}= 81.47° its corresponding angle θ_{i5} will be significantly lower than θ_c^{MM}. Thus, in order for a marginal ray to fall within the fiber acceptance cone, N=5 indicates an upper limit that should not be reached.

When the fiber is already spliced, the difference between the refractive indices (resin-silice) of the two media would be less abrupt, and the refracted rays in Figure 2 would roughly follow the dotted lines. In such a case, if the ray exits the CW without Fresnel reflection loss, it will fall within the acceptance cone of the MMF, but only if it undergoes no more than 5 TIR´s.

2.2. Simulation

To study the ray propagation in more detail within the CW, simulations were carried out using a CW design and component setup as shown in Figure 3 (a). To provide a comparison with the previous analysis, it was used the same parameters as in the earlier case, and the dimensions of the CW (a solid truncated cone with n=1.49) were as follows: C_{height}=50mm, ϕ_{top}=1mm and ϕ_{bottom}=5mm. A focused beam was used as the ray source, with an angular aperture corresponding to a lens NA ranging from 0.11 to 0.16, to match the data presented in Table 1. This setup simulates focused rays with an input angle θ_{input} similar to those shown in Figure 2, and also allows for the simulation of different mask diameters (MD).

Additionally, a circular planar annulus was positioned, with a 20mm stop aperture that matches the acceptance cone $\theta_{fiber} = 60°$. Thus, all rays exiting the CW and remaining within this cone would be those that could potentially be coupled to the MMF if it were included in the configuration.

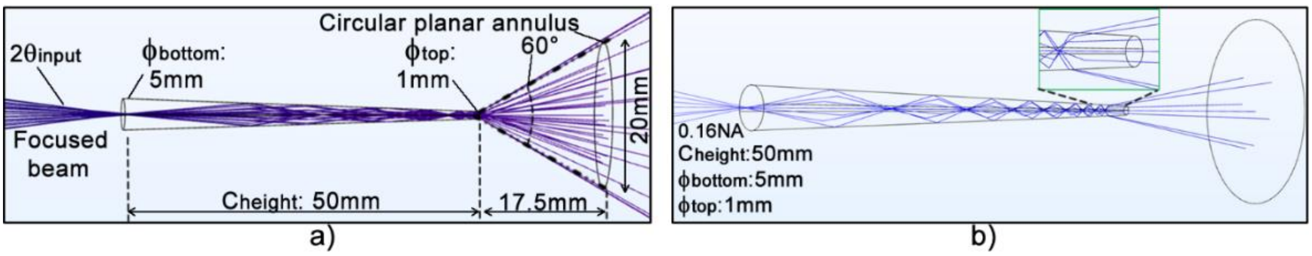

Figure 3.
(a) Set up used for the simulation of ray propagation in the CW; (b) Marginal ray tracing (0.16NA) to determinate the number of TIR´s for incident rays on the CW.

As shown in **Figure 3** (b), when using $\boldsymbol{NA_1}$=0.16, a marginal ray trace yields a total of 8 TIR's after which the rays begin to escape through the cone's wall. This indicates that any ray with an aperture close to that of the marginal rays will be susceptible to attenuation at the cone's sidewall. While the simulation shows escaping rays that are within an aperture smaller than the acceptance cone of the MMF, for these rays to be coupled to the MMF, it is essential that they also exit through the tip of the cone**.**

Figure 4 (a) illustrates the behavior of the previous case when the 0.16NA is filled with a larger number of rays uniformly distributed on the angle $\boldsymbol{\theta_{input}}$. As shown in **Figure 4** (b) and (c), applying aperture/stop filters at the end of the CW, helps to differentiate between leaked rays and those that exit through the tip of the cone. For this case, the attenuation losses within the CW are significant. Additionally, among the rays that manage to exit through the tip of the CW, a considerable portion exhibits an aperture that exceeds the MMF's acceptance cone.

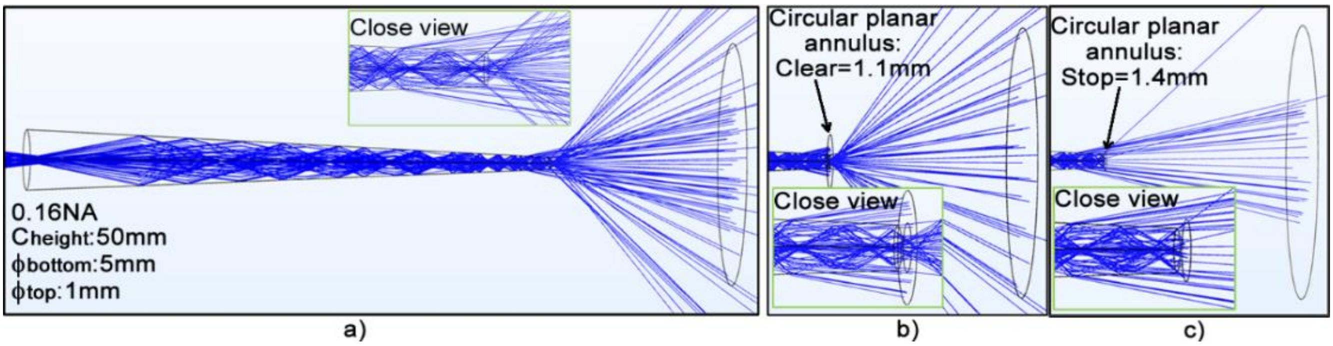

Figure 4.
(a) Rays' propagation in the CW when NA=0.16 is filled; (b) A 1.1 mm aperture was placed to isolate only the rays exiting from the cone tip; (c) A stop was used to isolate the rays exiting from the sidewall.

Subsequently, a marginal ray trace is performed using NA=0.11. As shown in Figure 5 (a), the marginal rays undergo 6 TIR´s before exiting the tip of the cone. This implies that the CW supports transmission of all the launched rays without any loss or attenuation due to Fresnel reflection at the sidewall.

As shown in Figure 5 (b), when the 0.11NA is filled with rays, it is observed that the CW does not exhibit losses due to lateral escape, however, a significant portion of the rays exiting its tip, exceeds the acceptance cone of the MMF. Figure 5 (c) shows what occurs if we launch a larger number of rays, this helps to visualize that ~30% of the total would be lost when CW is spliced with the MMF, as they exceed the MMF's acceptance cone.

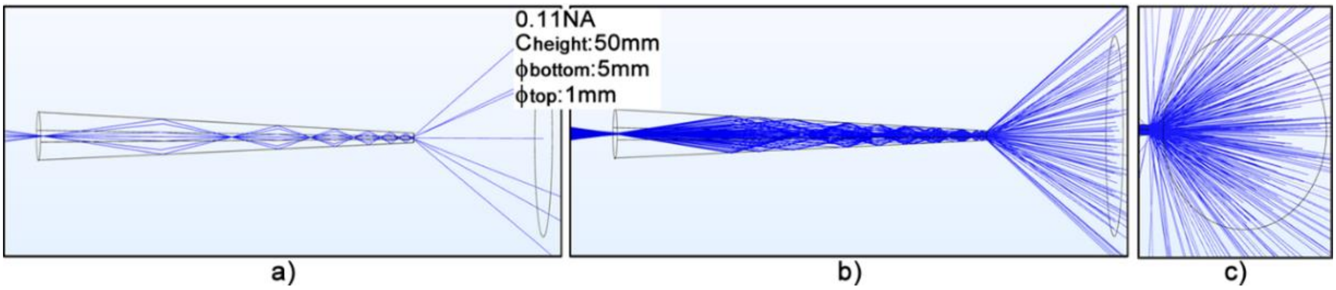

Figure 5.
(a) Marginal ray tracing (for 0.11NA) shows that the CW does not exhibit loss due to Fresnel reflection; (b) When filling the 0.11 NA with light, it is observed that all rays exit through the cone tip; (c) A close-up view allows an estimate that approximately 30% of the light from the CW falls outside the acceptance cone.

2.2. Conical Waveguide (CW) Manufacturing

Based on both the geometric analysis and simulations, we decided to manufacture the CW with dimensions C_{height}=50mm, ϕ_{top}=1mm and ϕ_{bottom}=5mm, for experimental validation. The design was first created in computer-aided design (CAD) software SolidWorks. Figure 6 (a) shows the 3D model of the CW, from which a 3D print was made using a CREALITY HALOT ONE printer. From the printed piece, a silicone mold was created, into which epoxy resin was poured. The epoxy resin used was a clear, general-purpose type for crafts, and multiple copies of the CW were manufactured using this method.

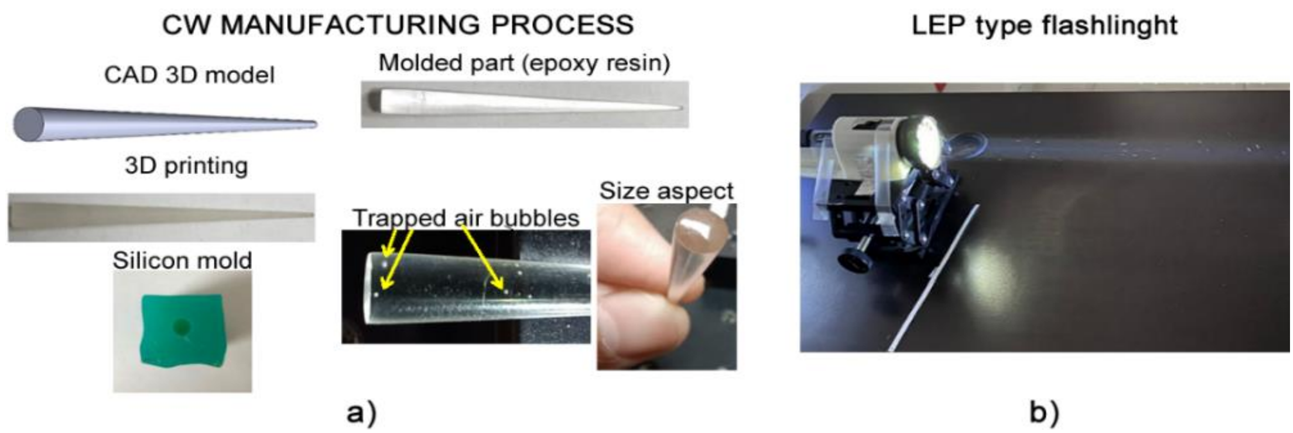

Figure 6.
(a) Manufacturing process of the CW based on a 3D model designed in CAD software; (b) Aspect of the beam launched by the LEP_type flashlight.

Manual polishing was performed to achieve a level of transparency sufficient for visible light transmission. Initially, the CW was 3D-printed in a translucent resin, and an attempt was made to polish this printed piece. However, significant challenges arose due to excessive air bubbles in the optical axis (produced by the additive process itself), which caused unwanted light scattering. As a result, the printed piece was used as a template to create a mold, and the resin casting method described earlier was employed instead.

Despite switching to resin casting, issues persisted, now in eliminating air bubbles formed during the mixing of the resin components. Consequently, the best-cast piece was selected from the batch, although it still displayed a few trapped air bubbles (see Figure 6 (a)). Once a CW was obtained that provided adequate transmission of visible light, testing began to direct light rays into the CW, concentrated by a FL (see schematic in Figure 1 (a)). Initially, a LED source was used, equipped with a lens and reflector array to collimate the light. However, the divergence was too high so that the FL could harness only a small fraction of the directed beam.

As shown in Figure 6 (b), a NITECORE P35i Dual Beam LEP flashlight, was used to address the previous issue, with an approximate divergence angle of ~2°, this light source, was used to launch collimated light rays with minimal divergence. For the experiments, the flashlight was operated in the highest intensity level, with a luminous flux of 410 lumens. This value was provided by the flashlight manufacturer and measured according to the ANSI/PLATO FL1-2019 international standard for flashlight testing under laboratory conditions.

3. Experimental Results

Ray trace simulations did not consider the finite size of the BSS that occurs experimentally. This is of central importance in our light collection system, as the focused BSS shouldn't exceed the diameter of the receiving CW (5 mm). Therefore, the flatness of the wavefront produced by our LEP-type flashlight at the time of reaching the FL is decisive for the size of the beam spot at the focal point, which seeks to be flat enough to produce a BSS as compact as possible. For this, a separation of several meters, referred to as torch distance (TD), is required between the flashlight and the FL.

As shown in Figure 7 (a), a setup for the direct measurement of the focused BSS was implemented for the TD/MD combinations. Figure 7 (b) shows that the intense brightness of the focused beam was reduced using a black surface, allowing a Vernier to measure the BSS. The inset image was captured using a camera filter to dim the intense glare of the spot. From the measurements it was found that for both TD<6 m and TD>8 m, a focused BSS>5 and a very expanded beam were obtained, respectively. Therefore, these TD values were discarded for this study.

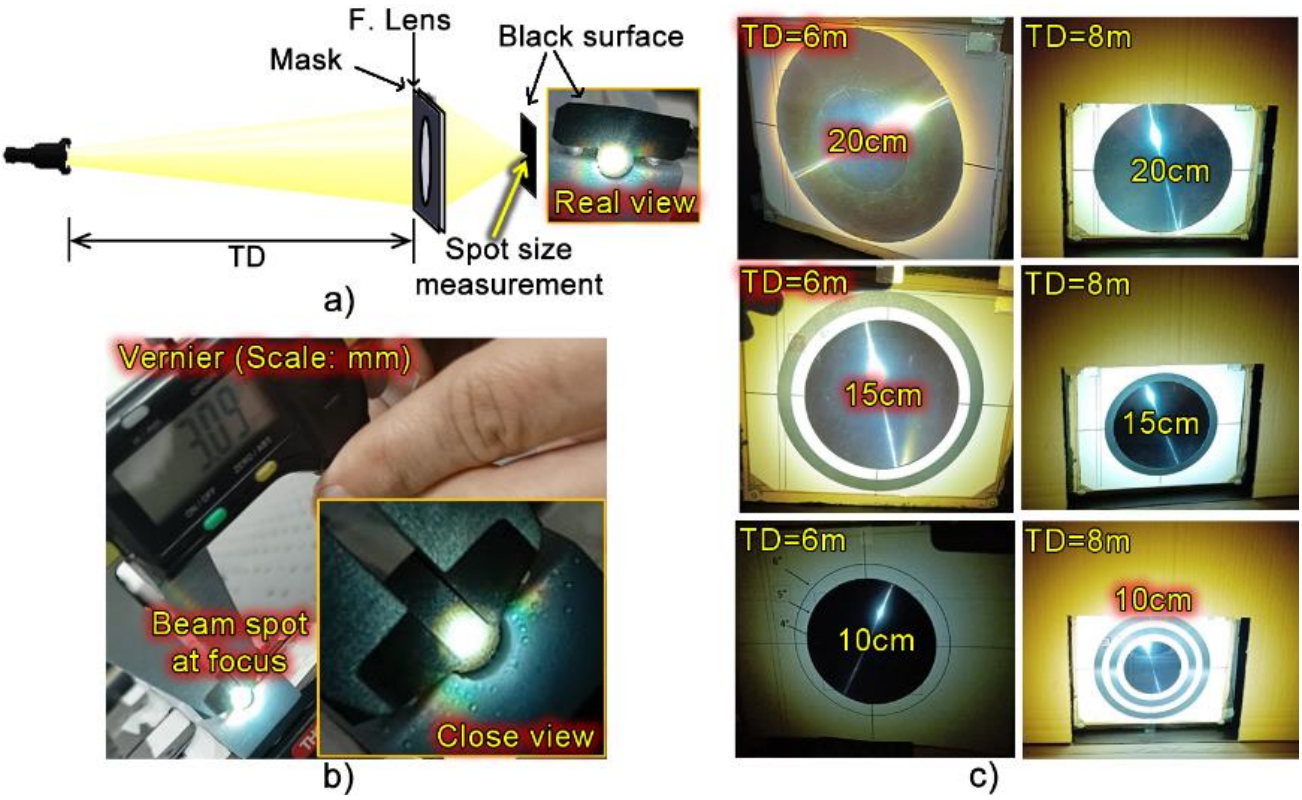

Figure 7.
(a) Setup for spot size measurement under varying TD and MD; (b) Vernier measurement corresponding to TD=8 m and MD=10 cm. The inset frame shows a BSS's close view; (c) Photograph of the masks with TD=6 m on the left and TD=8 m on the right.

On the other hand, it was found that for TD in the range of 6 m to 8 m, achieving a BSS of up to 3 mm was optimal and convenient. Table 2 shows a summary of these measurements, in this table, the diameter of the used mask is referred to as MD. As shown in Figure 7 (c) the masks reduce the amount of light passing through the FL. At TD=6 m, the flashlight beam completely covers the original diameter of the FL, while at TD=8 m, slightly exceeds the size of the FL.

The purpose of testing these TD/MD combinations was to compare their effects on both the BSS and lateral ray leakage as they deviated from the optimal configuration. Additionally, the information in Table 2 serves as a reference for the selection of FL characteristics and allows us to identify the optimal conditions (e.g. FL's size and NA, and indoor TD) for a minimum BSS.

Furthermore, Table 2 allows for the identification of experimental parameters that determine the launch light conditions (e.g., TD/MD, BSS). In fact, we used Table 2 as a reference procedure to conduct the optical characterization experiments for the FL-CW setup and later for the FL-CW-MMF setup. This enabled to provide an efficiency comparison that previewed the final impact on the expected trend of ray leakage, as well as the system's net efficiency.

Table 3.
Spot size for different combinations of TD and MD.

Mask Diameter (cm)	Spot size (mm) with TD=6m	Spot size (mm) with TD=8m
10	4.5	3
15	5.5	4
20	6.5	5

From Figure 8 (a) and (b), it may be noted the necessity to perform luminous flux measurements at this stage, specifically, the total flux exiting through the FL. This measurement is crucial for calculating the net efficiency of the collection system, as it represents the amount of light we intend to direct into the CW and subsequently into the MMF.

In this study, for all luminous flux measurements performed, the following method was used: a second FL (hereafter referred to as the projection lens) with a high NA (0.5 NA) and 10 cm focal length, was positioned to project the light onto a screen, creating a circle of approximately 90 cm in diameter over a short distance. Specifically, as illustrated in Figure 8 (a), the 0.5NA projection lens was placed a few centimeters before the focal point of the main FL (see inset photograph), allowing all the light to pass through the projection lens and be projected onto the screen.

As illustrated in Figure 8 (b), the luminous flux reaching this circle of light was calculated by summing the products of the area of each concentric ring (~3 cm in width) and its corresponding illumination in lux (a total of 15 readings taken along the radius of the circle). Given the radial symmetry of the light intensity distribution, it is assumed that the illumination recorded by the lux meter is constant within each concentric ring, provided the ring width is sufficiently narrow. This method is approximate, but it consistently showed reliable trends across all luminous flux measurements in this study.

Because the projection lens has a transmittance of approximately 90%, a compensation of ~11% should be added to the measured total calculated with this method. Subsequently, as shown in Figure 9 (a), the CW was positioned and aligned at the focal point, therefore the BSS coincided with its base area. The same methodology used to measure the FL's luminous flux was applied to the light emerging from the CW's tip. For this setup, the distance between the CW and the projection lens was ~2 cm. The resulting output flux allows the CW's efficiency to be determined by comparing it with the input flux.

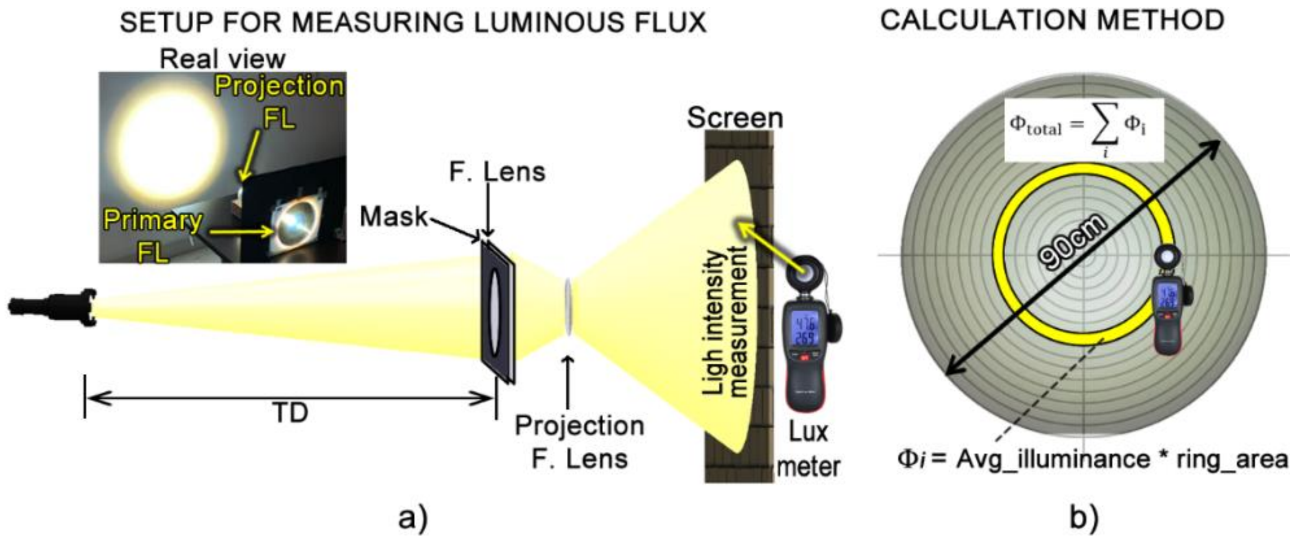

Figure 8.
(a) Setup for luminous flux measurement (by means of illuminance measurements) with the primary FL and a second projection FL; (b) Approximate calculation method for luminous flux.

The inset photograph at the bottom of Figure 9 (a), shows a thin aluminum sheet with a hole placed at the end of the CW. This setup blocks lateral glare from the CW, preventing this stray light from reaching the projection area and interfering with the illuminance measurements. It is worth mentioning that for this setup, we manufactured a custom 3D mount for the CW. However, the measurement of lumens to characterize the transmission efficiency of the CW requires that it be placed outside the mount in order to place the aluminum part.

Similarly, the top right inset photograph of Figure 9 (a) shows that any stray light from the FL that was not coupled into the CW was also blocked using a piece of cardboard, allowing only light directed toward the base of the cone to pass through. The photographs in Figure 9 (b) provide a visual comparison of the brightness produced by the lateral light leakage, which is observed near the tip of the cone. To consistently evaluate the difference in brightness between these images, a filter was applied to the digital camera sensor (Motorola Edge 20 Lite mobile phone). The filter settings were as follows: light sensitivity (ISO) = 100, shutter speed = 1/2000, white balance (color temperature) = 4495, and exposure compensation = disabled.

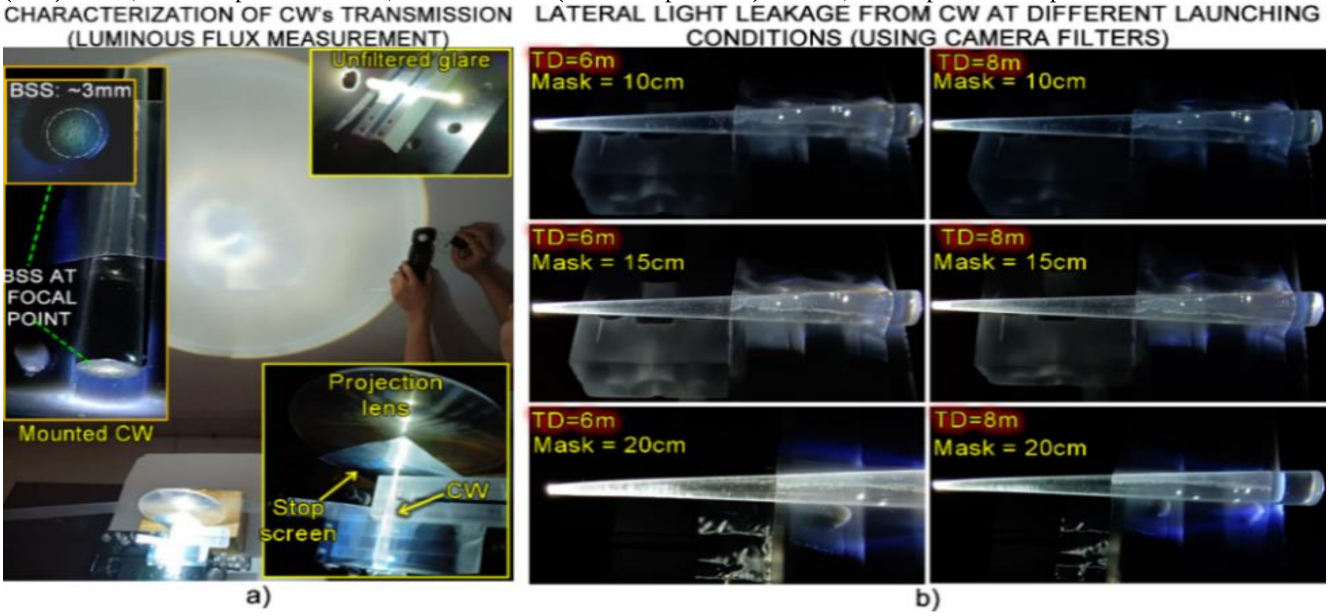

Figure 9.
(a) Illuminance measurements used to calculate the luminous flux exiting the CW. Inset frames: (left) BSS of the launched light from the FL, (upper right) intense (unfiltered) glare from CW at maximum power, (lower right) an aperture stop was placed to block sidewall light; (b) Sidewall leak comparison for different launching conditions.

The observed brightness corresponds to light leakage from rays. When comparing this result with the NA and spot size parameters in Table 3 a trend emerges, lower lens NA and smaller beam spot sizes result in reduced light leakage.

Once the CW was characterized, it was spliced with the MMF. Prior to splicing, the tips of both the CW and the MMF were carefully polished. Due to its larger diameter, the MMF required a special tool to make the cut. The used tool was a ruby fiber scribe (Thorlabs S90R), which, being a manual tool, required multiple attempts to achieve an acceptable result. Figure 10 (a) shows the appearance of the polished and aligned tips just before splicing. As seen, both pieces were placed in a custom 3D-printed mount designed to hold them on a 3-axis micrometric translation stage, allowing for precise alignment, application of a drop of adhesive, and joining at the appropriate moment.

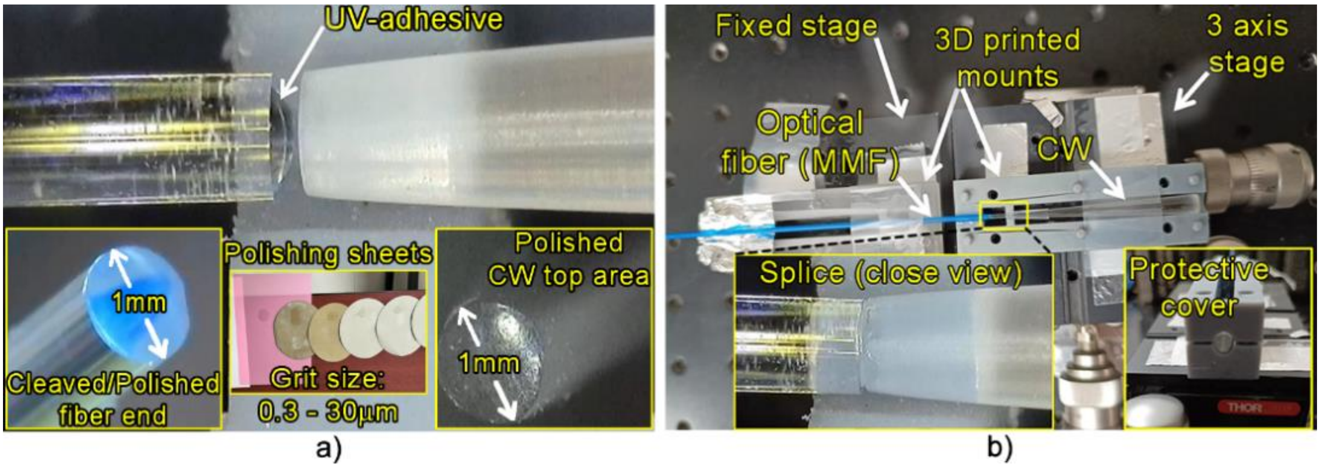

Figure 10. (a)
The CW and MMF tips were progressively polished, using a rage of grits from 30 µm to 0.3 µm and carefully aligned before splicing; (b) The general appearance of the spliced CW-MMF connection.

The figure also includes a cross-sectional view of the tips of each piece, as well as the sandpapers used for polishing. For bonding, a small drop of hard-type optical adhesive (refractive index n=1.49) was applied, which cures in 20 minutes under ~250 nm UV light from a 25W germicidal compact fluorescent lamp. Figure 10 (b) shows the result of the bond, with the inset images providing a close-up of the splice area. Following the splicing process, the assembly was mounted for characterization testing. As illustrated in Figure 11 (a), a laser level was employed to project reference lines, enhancing the alignment precision of the FL-CW-MMF assembly.

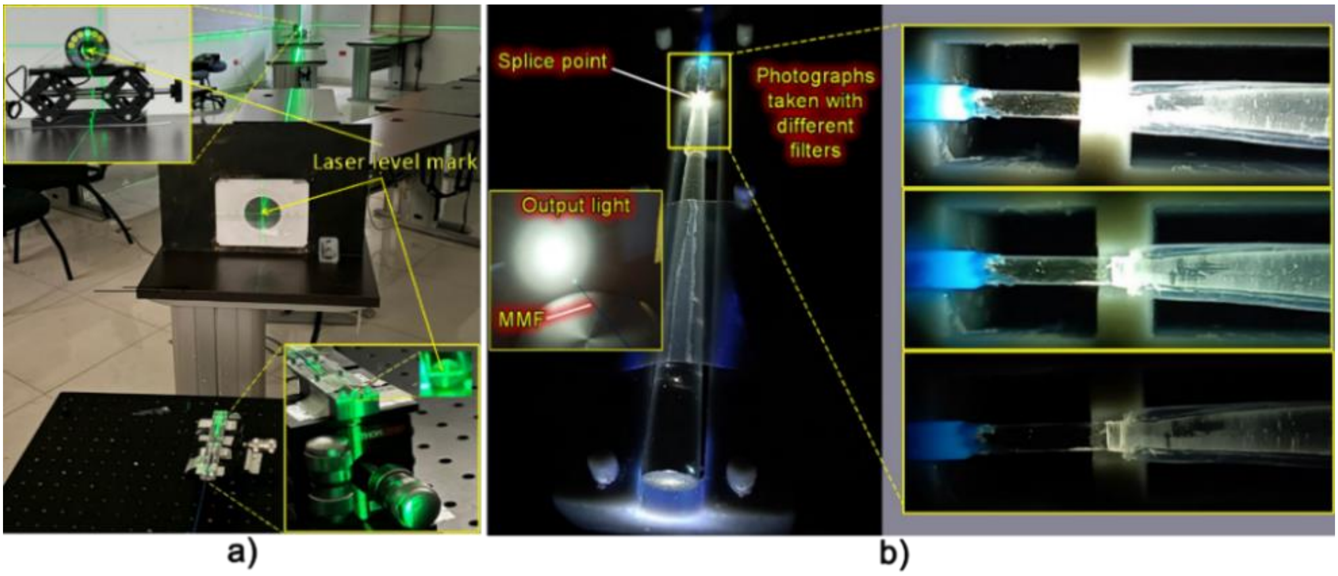

Figure 11.
(a) The setup alignment, using a laser level to align the components along the optical axis; (b) CW-MMF splice with the flashlight at full power and an image of the splice with different filters.

Figure 11 (b) illustrates various key areas of the CW-MMF assembly. These images correspond to the case when MD = 10 cm and TD = 8 m, with the flashlight operating at its maximum power. With the aim to assess the temperature effects resulting from resin absorption, light leakage, and splice induced-losses, a Fluke Ti100 thermal camera was used to capture thermal images. As shown in Figure 12 (a) The maximum recorded temperature was 41°C, measured at the hottest point. Moreover, the heat was predominantly concentrated on the CW side of the splice.

The luminous flux of the entire assembly was measured for various MD and TD using the same 0.5NA projection lens and measurement procedure. As depicted in Figure 12 (b), the MMF tip was placed approximately 3 cm away from the projection lens, resulting again in a projected beam diameter of 90 cm on the screen.

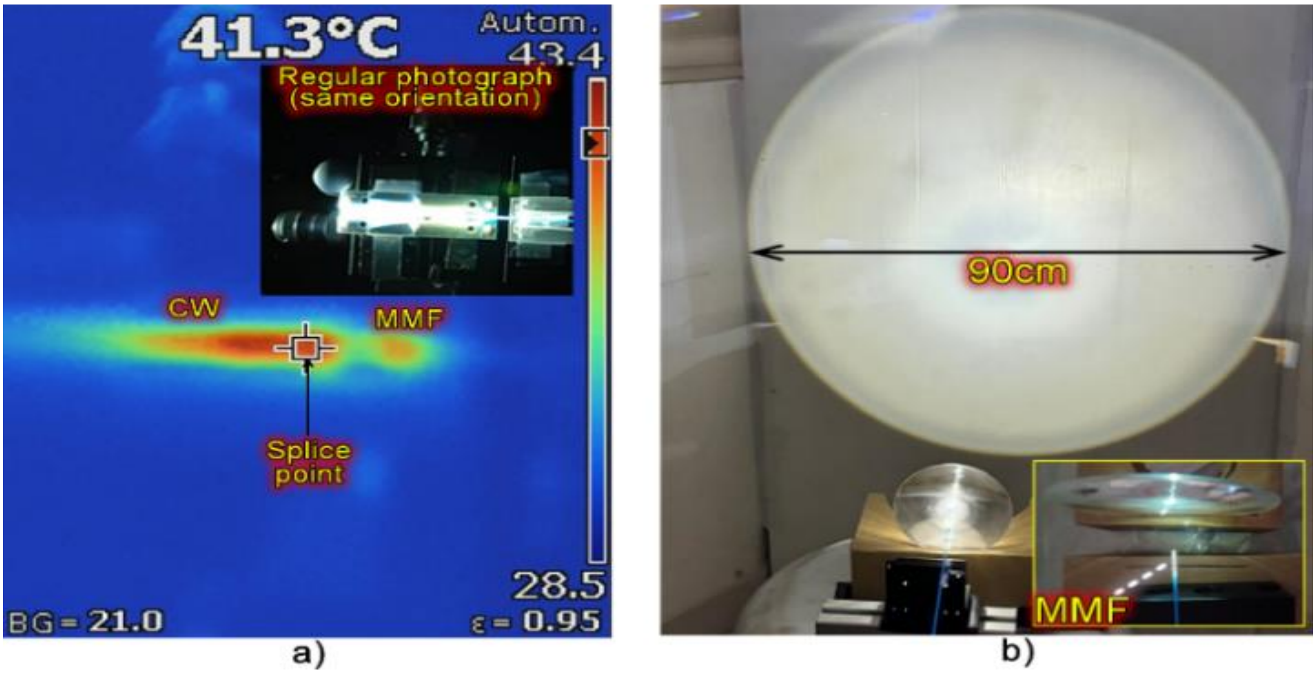

Figure 12.
(a) Thermal image of the splice zone. Inset image: Same (regular) photograph. (b) Setup for luminous flux measurement at the exit of the MMF.

Figure 13 summarizes the luminous flux measurement points mentioned, highlighting three key zones based on which light transmittance calculations were made. Also, emphasizes the importance of understanding the losses that occur during splicing. The first step is to determine the attenuation within the MMF, which corresponds to 20–60 dB/km in the visible spectrum (from manufacturer's specs). The following formula is used to calculate attenuation loss:

$$Attenuation(dB) = 10\log P_{out}/P_{in}\,, \tag{3}$$

where P_{in} and P_{out} are the input and output optical powers, respectively. For this experiment, considering that only 1 meter of fiber was used and applying the average attenuation value from the specified range (40 dB/km), an expected attenuation of 0.04 dB/m can be estimated. Thus P_{out}/P_{in}=0.9908. In percentage terms, this corresponds to an attenuation loss of 1% of the input power relative to the output for the 1-meter fiber segment used. For larger MMF lengths, if multiples of 10 meters were used, the output-to-input power ratio would be P_{out}/P_{in}= 0.912 @ 10 m, P_{out}/P_{in}= 0.831 @ 20 m, and so on.

Therefore, splice loss can be determined by knowing the optical powers of the luminous fluxes $B_{coupled}$ (the portion of rays from B within the MMF´s acceptance cone) and C, as indicated in Figure 13. Where it is known that C is 99% of the initial power accessing the MMF immediately after the splice, denoted as C_{INPUT} in the figure. For a 1-meter fiber, this can be expressed as:

$$Splice_{loss}(dB) = 10log\frac{C_{INPUT}}{B_{coupled}} = 10log\frac{1.01C}{B_{coupled}} \tag{4}$$

If a different fiber length is used, this splice loss formula should be recalculated and applied in the efficiency calculations of the collection system. Table 4 summarizes the measurement results for characterizing the transmission efficiency of the FL-CW and the FL-CW-MMF assemblies at the positions A, B, and C shown in Figure 13.

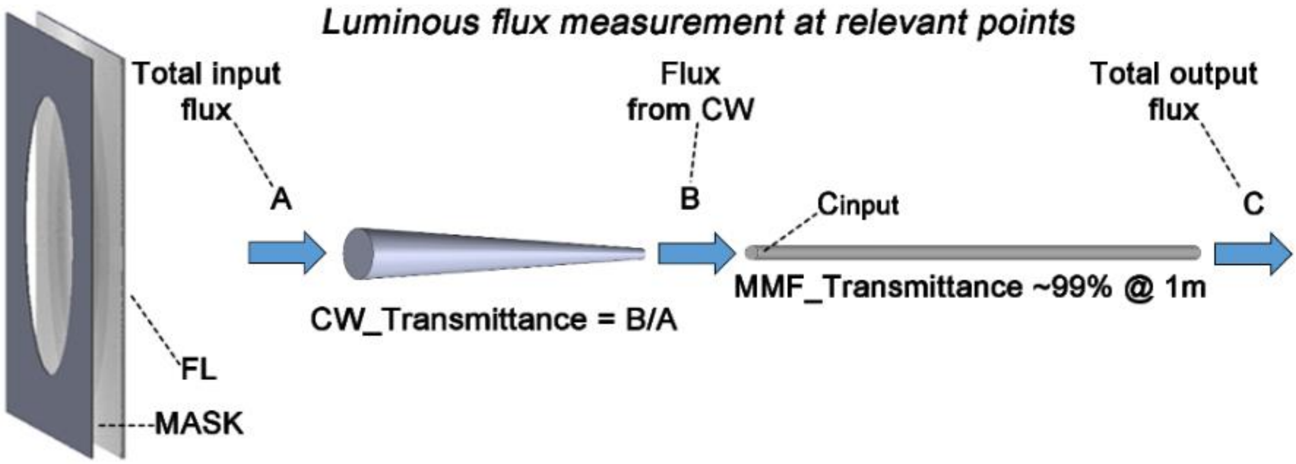

Figure 13.
Summary of the luminous flux measurements: The MMF length used is 1 m for all the experiments.

From Table 4, it can be observed that with smaller mask sizes, higher transmission efficiency is achieved. Among the cases from Table 4, the highest CW's throughput was 34.7% which also corresponded with the highest net efficiency 17% (achieved with a TD = 8 m, MD = 10 cm and a 0.11NA). In absolute terms, these efficiencies were obtained from an incoming luminous flux of ~60 lumens, which, after entering the CW, resulted in an output (B) of ~20 lumens. At the MMF output (C), there was a luminous flux of ~10 lumens, which corresponded to the 17% net efficiency.

Unlike the above-mentioned results, the simulation in Figure 5 (using the same NA_1 = 0.11) predicted a CW's throughput of 100% while experimentally, it was obtained only 34.7% of the input light. Similarly, for this same case, the simulation predicted that ~70% (net efficiency) of the rays exiting the CW would fall within the MMF's acceptance cone, however the corresponding experimental value was 17%. To analyze the causes of these deviations in efficiency values (experimental vs. simulated), a discussion is provided in the following section.

Table 4.
Summary of luminous flux at key points in the setup.

MD		TD	Luminous flux from CW input to MMF output				
			Input CW (A)	Output CW (B)	Throughput CW	Output MMF (C)	NET Efficiency %
20 cm	(0.21NA)	6m	279.3112	50.1	17.9%	23.4812055	8.40682563
20 cm		8m	185.3608	33.53	18.1%	16.1983656	8.73883021
15 cm	(0.16NA)	6m	177.5204	42.82	24.1%	20.8906483	11.7680268
15 cm		8m	115.7308	28.08	24.3%	13.7205915	11.8556093
10 cm	(0.11NA)	6m	101.6883	28.54	28.1%	16.3890602	16.1169576
10 cm		8m	60.0025	20.85	34.7%	10.2230564	17.0377175

4. Discussion

The results presented above indicate that the main source of optical attenuation occurred within the CW. Even in the best-case scenario, 66% of the light launched by the primary FL was lost as it passed through the CW. The following discussion addresses the origin of such attenuation, highlighting both intrinsic material factors and extrinsic factors of significance.

Figure 9 (a) and (b) allows to understand that the brightness emitted by the CW, resulted from light scattered at the CW' surface. Despite careful polishing, Figure 10 (a) reveals a noticeable difference between the clarity of the MMF material and that of our CW, indicating that any imperfections in the polishing process contribute to scattering.

Additionally, thermal images in Figure 12 (a) show that light absorption caused a temperature increase particularly near the cone tip where the light ray density is highest. While further research is needed to quantitatively determine the individual contributions of scattering and absorption to attenuation, the captured images clearly demonstrate their significant impact on light loss.

Another significant factor contributing to attenuation is the CW's geometry as well as the finite size of the focused BSS. The simulations were designed to operate in an MMF's overfilled NA regime, with approximately 30% of the launched rays (for a 0.11NA FL) exceeding the MMF's acceptance cone, as depicted in Figure 5 (c). This was based on assuming that the light launched into the CW, focused in a perfectly point-sized spot. However, considering the overall size of the CW, a significantly different outcome could be expected if the used BSS goes from a point-size one to a size of ~3mm or larger.

This finite spot size results in a variation in the number of reflections experienced by rays at different radial positions, as illustrated in Figure 14 (a). Rays farther from the optical axis, such as the blue ray, undergo more reflections and reach the leakage threshold (critical angle) earlier than those closer to the axis. This phenomenon, along with the reflections experienced by rays farther from the axis, contributes to the observed light leakage near the cone tip during the experiments.

Additionally, while using masks to reduce the NA proved useful to increase efficiency, determining its effect on the (experimental) geometrical-related loss observed in the CW, requires a more detailed simulation which consider the real BSS.

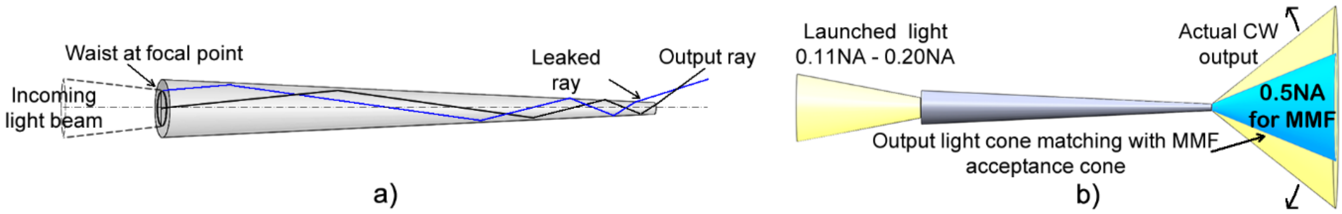

Figure 14.
(a) Illustration of the number of reflections experienced by rays at different radial positions (b) Schematic illustrating the concept of overfilling the NA of the receiving fiber.

Regarding the loss obtained after the CW-MMF splice, from the cases shown in Table 4, it is evident that as MD increases and TD decreases, the corresponding loss becomes greater. This can be explained by examining Figure 5 (c) and Figure 14 (b), which show that only the rays exiting the CW within the MMF's acceptance cone, can be coupled into the MMF. Consequently, under the experimental conditions for each case in Table 4, higher values of NA_1 result in a wider output aperture from the CW, leaving a larger proportion of rays outside the MMF's acceptance cone. This situation represents the primary source of attenuation observed at the splice.

Figure 14 (b) shows how to determinate the splice loss by measuring the luminous flux that falls within the acceptance cone for each case in Table 4. A stop aperture is placed at the CW output, allowing to measure only light within the MMF's acceptance cone. Then, the splice loss (and thus the percentage of power loss due to the splice) can be determined using Equation (4).

Despite the observed attenuation, this study has identified areas to improve the efficiency in our collection system, which opens up two interesting research directions: (i) optimizing the CW geometry to increase the system's net efficiency, and (ii) selecting the correct material for the CW that reduces scattering as well as heat. Additionally, this methodology can be applied to larger-diameter MMFs (e.g., 1.5 mm or greater).

Given the high power-handling capacity of a standard silica MMF in the visible spectrum (damage threshold specs ~250 kW/cm^2), the primary limitation on solar collection capacity for indoor illumination is the optical system's ability to couple light into the fiber core, a detailed study on this issue is proposed for future work.

5. Conclusions

A genuine CW design was successfully created based on geometric analysis and simulations and fabricated using an innovative process involving 3D resin printing and silicone molds. The CW was polished to achieve sufficient transparency for propagating visible light, resulting in an approximate output efficiency of 34.7%. Subsequent splicing with an MMF yielded a net efficiency of approximately 17% at the fiber output. This achievement was made possible by the careful development of a setup and alignment system, which included 3D-printed mounts, a 3-axis micrometric precision stage, a laser level, tape measures, and millimeter rulers, along with other precision tools to accurately align all components on the worktables.

This study allowed us to assess the feasibility of using the proposed continuous wave (CW). Its simplified collector manufacturing process reduced the cost and enabled the use of a silica multimode fiber (MMF) with low transmission loss over several tens of meters. Additionally, it established a successful design criterion and an experimental functional setup framework for the indoor characterization of a CW with the help of laser emission photonics (LEP) technology, providing a reference setup for evaluating the CW's suitability for outdoor use. This approach avoids prolonged exposure to sunlight for personnel conducting these tests and mitigates risks such as skin cancer and heatstroke.

Through the previous work, several areas of opportunity for future improvement have been identified. This research not only provides valuable insights into the performance of this specific CW design but also opens up possibilities for future investigations into a wider range of CW geometries. Moreover, the methodology and findings of this work can be used as a reference for future works such as solar tracking collectors or concentrators, development of optical devices, endoscopic applications and sensing.

References

[1] United Nations Department of Economic and Social Affairs, "United nations department of economic and social affairs," The Sustainable Development Goals Report 2024, UN, 2024.

[2] United Nations Environment Programme, *Bend the trend pathways to a liveable planet as resource use spikes*. Nairobi, Kenya: International Resource Panel, 2024.

[3] United Nations Environment Programme, "Global status report for buildings and construction: Beyond foundations - mainstreaming sustainable solutions to cut emissions from the buildings sector," *United Nations Environment Programme*, 2024. https://doi.org/10.59117/20.500.11822/45095

[4] N. A. Rahmany and M. H. Patmal, "Impact of solar heating technology installation on reduction of greenhouse gas emissions in Kabul city," *International Journal of Innovative Research and Scientific Studies,* vol. 4, no. 2, pp. 53-61, 2021. https://doi.org/10.53894/ijirss.v4i2.56

[5] M. Kunelbayev, M. Mansurova, G. Tyulepberdinova, T. Sarsembayeva, S. Issabayeva, and D. Issabayeva, "Comparison of the parameters of a flat solar collector with a tubular collector to ensure energy flexibility in smart buildings," *International Journal of Innovative Research and Scientific Studies,* vol. 7, no. 1, pp. 240-250, 2024. https://doi.org/10.53894/ijirss.v7i1.2605

[6] A. M. Waseel, N. R. Sabory, H. Zaheb, and A. K. Waseel, "Central heating by seasonal sensible heat storage of solar thermal energy," *International Journal of Innovative Research and Scientific Studies,* vol. 4, no. 2, pp. 100-110, 2021. https://doi.org/10.53894/ijirss.v4i2.63

[7] A. A. Amiri, "Comparative analysis of economic aspects of concentrated solar power versus photovoltaic in afghanistan-case study: Kang district, nimruz," *International Journal of Innovative Research and Scientific Studies,* vol. 4, no. 2, pp. 111-119, 2021. https://doi.org/10.53894/ijirss.v4i2.64

[8] IEA, *Energy efficiency*. Paris: IEA, 2023.

[9] United Nations Environment Programme, "Model regulation guidelines for energy efficiency and functional performance requirements for general service lamps and linear lighting supporting information," Retrieved: https://united4efficiency.org/resources/model-regulation-guidelines-for-energy-efficiency-and-functional-performance-requirements-for-general-service-lamps-and-linear-lighting-supporting-information/, 2021.

[10] United Nations Environment Programme, "Accelerating the global adoption of energy-efficient lighting," United Nations Environ. Program, 2017.

[11] IEA, "Net Zero by 2050, IEA," Retrieved: https://www.iea.org/reports/net-zero-by-2050, 2021.

[12] M. Zhao and T. Miyamoto, "Efficient LED-array optical wireless power transmission system for portable power supply and its compact modularization," *Photonics,* vol. 10, p. 824, 2023. https://doi.org/10.3390/photonics10070824

[13] G. Zissis, "Energy consumption and environmental and economic impact of lighting: The current situation," *Handbook of Advanced Lighting Technology,* pp. 1-13, 2016. https://doi.org/10.1007/978-3-319-00176-0_40

[14] N. Gentile *et al.*, "Evaluation of integrated daylighting and electric lighting design projects: Lessons learned from international case studies," *Energy and Buildings,* vol. 268, p. 112191, 2022. https://doi.org/10.1016/j.enbuild.2022.112191

[15] N. H. Moadab, T. Olsson, G. Fischl, and M. Aries, "Smart versus conventional lighting in apartments-Electric lighting energy consumption simulation for three different households," *Energy and Buildings,* vol. 244, p. 111009, 2021. https://doi.org/10.1016/j.enbuild.2021.111009

[16] J.-c. Hsieh, "Study of energy strategy by evaluating energy–environmental efficiency," *Energy Reports,* vol. 8, pp. 1397-1409, 2022. https://doi.org/10.1016/j.egyr.2021.12.061

[17] N. Gentile, "Improving lighting energy efficiency through user response," *Energy and Buildings,* vol. 263, p. 112022, 2022. https://doi.org/10.1016/j.enbuild.2022.112022

[18] B. R. Sutherland, "Lighting policies spur global innovation," *Joule,* vol. 3, no. 3, pp. 639-640, 2019. https://doi.org/10.1016/j.joule.2019.03.002

[19] U. Zia, S. Qureshi, H. Aslam, and M. Zulfiqar, "Driving parameters for technology penetration in pakistan: A case study for indoor led lighting," *Engineering Proceedings,* vol. 23, no. 1, p. 10, 2022. https://doi.org/10.3390/engproc2022023010

[20] Y. Wang, X. Hong, D. Wu, H. Wu, and A. Ishibashi, "Cylindrical waveguides and multi-junction solar cell investigated for two-dimensional photorecepto-conversion scheme," in *Photonics. https://doi.org/10.3390/photonics10030299.*, 2023, vol. 10, no. 3, p. 299.

[21] F. Bodem, "The limits to incoherent optical power launching into lightguides," *Optics & Laser Technology,* vol. 10, no. 2, pp. 89-96, 1978. https://doi.org/10.1016/0030-3992(78)90103-2

[22] P. M. Viera-González, G. Sánchez-Guerrero, D. E. Ceballos-Herrera, and R. Selvas-Aguilar, "Radiant flux analysis of a system based in imaging fresnel lens and plastic optical fiber with fiber lenses," *Res. Comput. Sci.,* vol. 131, pp. 119-124, 2017.

[23] G. E. Arnaoutakis, J. Marques-Hueso, T. K. Mallick, and B. S. Richards, "Coupling of sunlight into optical fibres and spectral dependence for solar energy applications," *Solar Energy,* vol. 93, pp. 235-243, 2013. https://doi.org/10.1016/j.solener.2013.04.008

[24] N. H. Vu, T. T. Pham, and S. Shin, "Large scale spectral splitting concentrator photovoltaic system based on double flat waveguides," *Energies,* vol. 13, no. 9, p. 2360, 2020. https://doi.org/10.3390/en13092360

[25] R. Neale *et al.*, "The effects of exposure to solar radiation on human health," *Photochemical & Photobiological Sciences,* vol. 22, no. 5, pp. 1011-1047, 2023. https://doi.org/10.1007/s43630-023-00375-8

[26] The Effect of Occupational Exposure to Solar Ultraviolet Radiation on Malignant Skin Melanoma and Non-Melanoma Skin Cancer, *A systematic review and meta-analysis from the who/ilo joint estimates of the work-related burden of disease and injury*. Geneva: World Health Organization, 2021.

[27] A. Grigore, A.-M. Oproiu, I. Iancu, and I.-P. Florescu, "The immune response of cutaneous basosquamous-and squamous-cell carcinoma associated with sun exposure," *Current Oncology*, vol. 31, no. 5, pp. 2481-2487, 2024. https://doi.org/10.3390/curroncol31050185

[28] K. Wunderlich, M. Suppa, S. Gandini, J. Lipski, J. White, and V. Del Marmol, "Risk factors and innovations in risk assessment for melanoma, basal cell carcinoma, and squamous cell carcinoma," *Cancers*, vol. 16, no. 5, p. 1016, 2024. https://doi.org/10.3390/cancers16051016

[29] C. Symanzik and S. M. John, "Prevention of occupational skin cancer caused by solar ultraviolet radiation exposure: Recent achievements and perspectives," *Dermato*, vol. 4, no. 2, pp. 46-59, 2024. https://doi.org/10.3390/dermato4020006

[30] M. Brandlmaier, M. Hoellwerth, P. Koelblinger, R. Lang, and A. Harrer, "Adjuvant PD-1 checkpoint inhibition in early cutaneous melanoma: immunological mode of action and the role of ultraviolet radiation," *Cancers*, vol. 16, no. 8, p. 1461, 2024. https://doi.org/10.3390/cancers16081461

[31] B.-M. Chen, S.-P. Ying, T. A. Pham, S.-Y. Tseng, and Y.-K. Chang, "The development of a remote edge-lit backlight structure with blue laser diodes," *Photonics*, vol. 11, p. 78, 2024. https://doi.org/10.3390/photonics11010078

[32] N. H. Vu, T. T. Pham, and S. Shin, "LED uniform illumination using double linear Fresnel lenses for energy saving," *Energies*, vol. 10, no. 12, p. 2091, 2017. https://doi.org/10.3390/en10122091

[33] O. R. Abdullaev, A. V. Aluev, Y. L. Akhmerov, N. y. V. Kourova, M. V. e. Mezhennyi, and A. Chelny, "White light source with laser-excited phosphor," *Quantum Electronics*, vol. 47, no. 10, pp. 927-931, 2017. https://doi.org/10.1070/QEL16396

[34] C. Cozzan *et al.*, "Stable, heat-conducting phosphor composites for high-power laser lighting," *ACS applied materials & interfaces*, vol. 10, no. 6, pp. 5673-5681, 2018. https://doi.org/10.1021/acsami.8b00074

[35] A. Lenef, M. Raukas, J. Wang, and C. Li, "Phosphor performance under high intensity excitation by InGaN laser diodes," *ECS Journal of Solid State Science and Technology*, vol. 9, no. 1, p. 016019, 2019. https://doi.org/10.1149/2.0352001JSS

[36] R. A. Osborne, N. J. Cherepy, P. S. Bleier, R. M. Gaume, and S. A. Payne, "Phosphor ceramic composite for tunable warm white light," *Materials*, vol. 17, no. 13, p. 3187, 2024. https://doi.org/10.3390/ma17133187

[37] F. Chen, M. N. Akram, and X. Chen, "Novel Red-Emitting Eu^{3+}-Doped $Y_2(W_xMo_{1-x}O_4)_3$ Phosphor with High Conversion Efficiency for Lighting and Display Applications," *Molecules*, vol. 28, no. 12, p. 4624, 2023. https://doi.org/10.3390/molecules28124624

[38] M. Yan, M. Gong, and J. Ma, "High extraction efficiency phosphor design applied in laser lighting," *Optics Express*, vol. 31, no. 2, pp. 1190-1201, 2023. https://doi.org/10.1364/OE.479070

[39] G. Brooker, *Modern classical optics*. New York: Oxford University Press, 2003.